Archives of Hydro-Engineering and Environmental Mechanics 71 (2024), pp. 135–157, doi: 10.2478/heem-2024-0009

sciendo

ARCHIVES OF HYDRO-ENGINEERING AND ENVIRONMENTAL MECHANICS

Published since 1954 ISSN 1231–3726

Depth-Averaged Modeling of Skimming Flow over a Bevel-Shaped Stepped Spillway

Yebegaeshet T. Zerihun

David & James – Engineering and Environmental Consultancy, 204 Albion Road, Vic 3350, Australia; e-mail: zyebegaeshet@gmail.com

(Received 16 November 2024; revised 06 January 2025)

Abstract. The air-water flow properties of skimming flow over a moderately sloping stepped spillway with beveled-face steps were investigated using a non-hydrostatic depth-averaged mixture flow model. The proposed model couples the Boussinesq-type equations with the depth-averaged air transport equations. Additionally, it incorporates a depth-averaged $k-\varepsilon$ turbulence model to deal with the turbulent issue of the self-aerated flow. The numerical solutions of these higher-order equations were obtained by means of a hybrid finite-volume and finite-difference scheme and were validated with a set of data from large-scale experiments. For the flow condition considered, the simulation results closely correlated with the experimental data, thereby demonstrating the model's capacity for capturing the effects of air entrainment on the dynamic characteristics of the flow. Furthermore, the energy dissipation performance of the stepped spillway was examined. The results attested that the total energy loss decreases as the drop number increases, highlighting the link between the loss of the flow's kinetic energy and the variation of the spillway discharge. With the established acceptable accuracy, the proposed model is well suited to analyzing the mean flow characteristics of aerated flow in such a type of stepped chute.

Key words: stepped spillway, skimming flow, energy dissipation, aerated flow, finite-volume method, non-hydrostatic model

1. Introduction

Climate and land use changes significantly affect the hydrology of the catchment by altering the magnitude and frequency of the extreme rainfall and runoff events as well as the loads from the catchment sediment yield. Because of these, existing old embankment dams do not satisfy the current higher standard design criteria. Their spillways do not have adequate capacity to safely discharge the inflow design flood; they are hydrologically deficient. Roller-compacted concrete (RCC) stepped spillway, which enhances energy dissipation, is commonly used as an overlay to rehabilitate and modernize these dams. Recently, a bevel-shaped stepped spillway with a linear crest has been implemented to protect the dams against overtopping erosion and breach.

It also provides additional spillway discharge capacity and overcomes the drawbacks of a square-edged vertical face stepped spillway. Fig. 1 shows a typical application of RCC overtopping protection to hydraulically upgrade the Leyden Dam in USA. Numerical simulation of turbulent flow over this type of structure involves computations of the local aerated flow parameters and the associated energy dissipation rate by treating the complex three-dimensional (3D) flow as a planar two-dimensional (2D) open-channel flow. The horizontal length scale of such a 2D flow problem is much shorter than the flow depth. The proposed 2D modeling approach maintains a balance between the requirements of computational efficiency and accuracy, and its results provide vital information to support full 3D modeling. It is the plan of this study to perform such a type of modeling task by applying a higher-order depth-averaged mixture flow model.

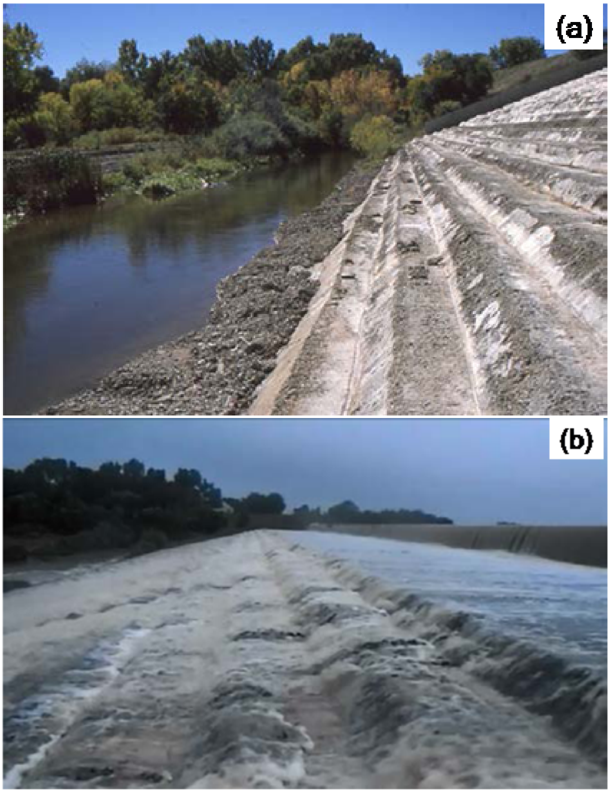

Fig. 1. (a) The auxiliary stepped spillway of the Leyden Dam in Colorado, USA; and (b) overtopping flow along the chute during a storm event (after Hansen and Fitzgerald 2016)

For analyzing two-phase flow problems, a number of investigations have been recently performed to extend the lower- and higher-order hydrodynamic models. For practical problems with a large computational domain such as aerated flows over hydraulic structures, it is computationally uneconomical to directly resolve the tiny scale motion of air bubbles, turbulent eddies, and free-surface variations using higher-order models. The common practice is to adopt grid-based variables for the dynamics of air-water interaction and to resolve such local flow features on a relatively larger scale. This approach has been widely applied to enhance open-channel flow models. Based on the lower-order energy equation, a one-dimensional (1D) model, which accounts for the effects of aeration, was develop to simulate self-aerated flow over a hydraulic structure (Wahl and Falvey 2022). The model employed empirical equations stemming from experimental studies to predict the air concentrations. However, the application of the model is limited to a hydrostatic flow situation, where the effects of the streamline curvature and turbulence are insignificant. Following the method of Sene (1988) for approximating the source term, Ma et al (2011) introduced a sub-grid air entrainment module based on the turbulent kinetic energy and the velocity gradient normal to the free surface. This module was implemented into a computational multiphase fluid dynamics solver for the Reynolds averaged two-fluid equations. Castro et al (2016) too introduced an air entrainment module, where bubbles are entrained into the flow by vortices interacting with a free surface. Their module roughly estimated the total rate of bubble entrainment by a linear superposition of the contributions of each vortex. The authors of both studies (Ma et al 2011, Castro et al 2016) examined the validity of the approaches for self-aerated open-channel flows and obtained satisfactory results when compared with the experimental data. Using a similar mathematical approach as that of Ma et al, Lopes et al (2017) proposed a sub-grid module that added an extra advection-diffusion equation to the volume of fluid formulation to simulate the dispersed bubbles. An air entrainment module, which was based on a balance of turbulence, gravity, and surface tension effects, was also developed and incorporated into a commercial software package FLOW-3D (Hirt 2003, Souders and Hirt 2004). Within the framework of the Reynolds-averaged Navier-Stokes (RANS) equations, Zabaleta et al (2023) proposed a numerical model for analyzing self-aerated flow problems. The model implemented a three-phase mixture approach, which was composed of a continuous air, bubble, and water phases. This approach resulted in complex system of equations. Consequently, their model may not be computationally efficient to solve large-scale flow problems.

In addition to the above considerable work, the structures of skimming flow in the aerated (Lopes et al 2017, Almeland et al 2021) and non-aerated (Bombardelli et al 2011, Bayon et al 2018) regions of a stepped spillway with vertical face steps were thoroughly investigated using a higher-order numerical approach. However, no extensive studies have been performed so far for examining the salient features of turbulent aerated flow over a bevel-shaped stepped spillway using a RANS equations-based model. As noted by several investigators (e.g., Chinnarasri and Wongwises 2004, Relvas and Pinheiro 2008, Zhang and Chanson 2018), the step geometry substantially affects the turbulent structures of the mixture flow and hence the development of the point of incipient aeration. Therefore, the current study is different from previous studies, which investigated the hydraulics of a square-edged vertical face stepped chute, and is relevant to modern design practice of embankment dam stepped spillways.

The aim of this study is two-fold. First, an alternative higher-order model for skimming flows over a bevel-shaped stepped spillway is developed by coupling the depth-averaged Boussinesq-type equations (Zerihun 2024) with a depth-averaged air transport equation that incorporates a source term to quantify the self-aeration process. The proposed mixture flow model is capable of predicting the mean and bottom air concentrations besides the local flow characteristics of the turbulent flow with curvilinear streamlines. As noted by Zerihun (2021), the existing higher-order depth-averaged hydrodynamic models underestimate the free-surface elevations of a free hydraulic jump partly due to the lack of a correction term for the effects of air entrainment. This drawback can be easily overcome by the current model. The second aim is to explore the model's capability for simulating the important aspects of the aerated open-channel flow along the stepped chutes by comparing its solutions with the experimental data. The results of this part of the study enable us to examine the overall hydraulic performance of such types of structures with finite bed slopes. It is important to note that the numerical model proposed here ignores the bubble breakup and coalescence processes.

The outline of the paper is as follows: first, a brief summary of the derivation of the governing equations is given in Section 2, followed by a comprehensive discussion of the main features of the hybrid numerical scheme (Section 3). In Section 4, a detailed description of the results of the model for the problem of a skimming flow is presented. Finally, Section 5 discloses the main findings of this study.

2. Development of the Mathematical Model

2.1. Hydrodynamic Equations

For a fluid-sediment mixture flow, Zerihun (2024) developed a non-hydrostatic model by depth averaging the continuity and the RANS momentum equations. The equations of this model for an air-water mixture flow (see Fig. 2) in a rigid-bed rectangular channel ($\partial Z/\partial t = 0$) can be written in the following form:

$$\frac{\partial H}{\partial t} + \frac{\partial q}{\partial x} = -\frac{1}{\rho}\left(q\frac{\partial \rho}{\partial x} + H\frac{\partial \rho}{\partial t}\right), \tag{1}$$

$$\begin{aligned}&\frac{\partial}{\partial t}(\rho q) + \frac{\partial}{\partial x}\left(\frac{\rho q^2}{H}\beta_1 + \frac{\rho g H^2}{2}\right) - \frac{\partial}{\partial x}\left(H\overline{\sigma}_x\right)\\&+ (\rho g H + p_D)\frac{\partial Z}{\partial x} + \frac{\partial}{\partial x}\left(\frac{H p_D}{2}\right) + \tau_b = 0,\end{aligned} \tag{2}$$

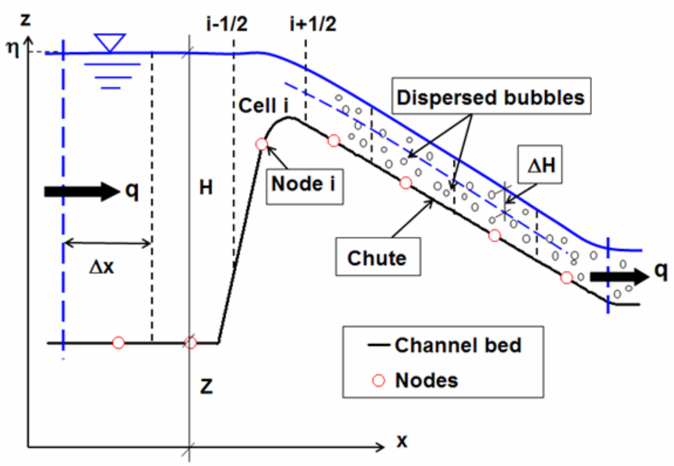

Fig. 2. Schematic representation of a 2D self-aerated open-channel flow

$$\frac{\partial}{\partial t}\left[\rho q\left(\beta_4\frac{\partial H}{\partial x}+\frac{\partial Z}{\partial x}\right)+\rho\beta_3 H\frac{\partial H}{\partial t}\right]$$
$$+\frac{\partial}{\partial x}\left[\rho\left[\frac{q^2}{H}\left(\beta_2\frac{\partial H}{\partial x}+\beta_1\frac{\partial Z}{\partial x}\right)\right]+\frac{q\rho}{2}\frac{\partial H}{\partial t}\right] \tag{3}$$
$$-\frac{\partial}{\partial x}(H\overline{\tau}_{zx})-p_D+\tau_b\frac{\partial Z}{\partial x}=0,$$

where x and z are the horizontal and vertical coordinates, respectively; τ_b is the bed shear stress; $\overline{\sigma}_x$ and $\overline{\tau}_{zx}$ are the depth-averaged normal and tangential stresses, respectively; q is the discharge per unit width; H is the mixture flow depth; g is acceleration due to gravity; ρ is the density of the air-water mixture; Z is the channel bed elevation; t is the time; p_D is the dynamic pressure at the channel bed; $\beta_1=\left(\omega^2-2\omega+4\right)/3$; $\beta_2=\left(\omega^2-4\omega+6\right)/6$; $\beta_3=(\omega+2)/6$; and $\beta_4=(4-\omega)/6$. The turbulent stress terms appearing in the above equations require a depth-averaged turbulence closure model, which will be briefly described in the next section. The distributions of the horizontal and vertical velocities are expressed by the following equations:

$$u=\frac{q}{H}\left(2\Lambda(1-\omega)+\omega\right), \tag{4a}$$

$$w = \frac{\partial H}{\partial t}\left(1-\omega(1-\Lambda)-(1-\omega)\left(1-\Lambda^2\right)\right)+\frac{q}{H}\frac{\partial\eta}{\partial x}(2-\omega)$$
$$-\frac{2q}{H}\frac{\partial Z}{\partial x}\left((1-\omega)(1-\Lambda)\right)-\frac{q}{H}\frac{\partial H}{\partial x}\left((1-\Lambda)\omega\right) \tag{4b}$$
$$-\frac{2q}{H}\frac{\partial H}{\partial x}\left((1-\omega)\left(1-\Lambda^2\right)\right),$$

$$\Lambda = \frac{z - Z}{\eta - Z}, \tag{4c}$$

where u and w denote the horizontal and vertical velocity components, respectively; ω is the velocity distribution parameter; Λ is a non-dimensional vertical coordinate; z is the vertical coordinate of a point in the flow field; and η is the free-surface elevation.

The density of the mixture flow may vary in the x-direction, but it is assumed to be independent of the vertical z-coordinate. Hence, it can be expressed as a function of the volumetric concentration as follows:

$$\rho = \rho_w (1 - C_m) + \rho_a C_m, \tag{5}$$

where ρ_w and ρ_a are the densities of clear water and air, respectively, and C_m is the depth-averaged or mean air concentration, denoting the average amount of bubbles dispersed in the water. Compared to those equations for single-phase flows, the effect of air transport phenomenon is taken into account by the density and dynamic viscosity parameters. The bed shear stress is reckoned using the Gauckler–Manning equation as follows:

$$\frac{\tau_b}{\rho} = \frac{g n_m^2 q^2}{R_H^{1/3} H^2} \left[1 + \left(\frac{\partial Z}{\partial x} \right)^2 \right], \tag{6}$$

where n_m is the Gauckler–Manning roughness coefficient, and R_H is the hydraulic radius of a section normal to the bed. It is known that self-aeration causes flow resistance reduction. This effect can be accounted for by applying an empirical correction factor (see Chanson 1994, Boes and Hager 2003b). In the governing equations, the mixture flow depth and the mean air concentration are computed based on the upper limit air concentration of 90%. The vertical profile of the pressure distribution can be expressed as (Zerihun 2024)

$$p = (\rho g H + p_D)(1 - \Lambda), \tag{7}$$

where p is the total pressure. As in the equations of Zerihun (2016), the effects of the steep slope of a channel are implicitly incorporated in the above equations. By ignoring the effects of the dynamic pressure ($w = 0$ and $p_D = 0$), a 1D shallow-water model can be recovered from these equations.

2.2. Turbulence Model

In order to account for turbulence effects, the Boussinesq hypothesis that relates the Reynolds stresses with a mean strain-rate tensor by eddy viscosity is employed here. Ignoring the effects of air concentration, the following expressions for the depth-averaged normal and tangential stresses are obtained from the Boussinesq (1877) equation:

$$H\overline{\sigma}_x = 2\left(\mu + \bar{\xi}\right)\left(\frac{\partial q}{\partial x} - \frac{q}{H}(2 - \omega)\frac{\partial \eta}{\partial x}\right) - \frac{2}{3}\rho H \bar{k}, \tag{8}$$

$$H\bar{\tau}_{zx} = \left(\mu + \bar{\xi}\right)\left[\frac{\partial}{\partial x}\left(q\left(\beta_4\frac{\partial H}{\partial x} + \frac{\partial Z}{\partial x}\right) + \beta_3 H\frac{\partial H}{\partial t}\right)\right] + \left(\mu + \bar{\xi}\right)\left[\frac{q}{H}(2-\omega)\frac{\partial \eta}{\partial x}\right], \tag{9}$$

where $\bar{\xi}$ and $\bar{k}$ are the depth-averaged eddy viscosity and turbulent kinetic energy, respectively, and μ is the molecular dynamic viscosity of the air-water mixture. The above expressions for the turbulent stresses are added to the governing equations as source terms. Several turbulence models, including the depth-averaged parabolic eddy-viscosity model, the mixing length model, and the renormalization group (RNG) $k-\varepsilon$ turbulence model (Yakhot and Orszag 1986), are introduced in the literature. In this study, the depth-averaged form of the standard $k-\varepsilon$ turbulence model (Jones and Launder 1972) is used. According to this model, the eddy viscosity is computed by the following equation:

$$\bar{\xi} = \rho\frac{C_\mu \bar{k}^2}{\bar{\varepsilon}}, \tag{10}$$

where $C_\mu = 0.09$. The turbulent kinetic energy and its dissipation rate, $\bar{\varepsilon}$, are determined by modifying the depth-averaged type of the $k-\varepsilon$ turbulence model, which was developed by Rastogi and Rodi (1978), for a 2D vertical plane flow problem. The resulting equations read as

$$\frac{\partial}{\partial t}\left(\rho H\bar{k}\right) + \frac{\partial}{\partial x}\left(\rho H\overline{U}\bar{k}\right) = \frac{\partial}{\partial x}\left[\left(\mu + \frac{\bar{\xi}}{\sigma_k}\right)H\frac{\partial \bar{k}}{\partial x}\right] + \rho H\left(P_H\frac{\bar{k}^2}{\bar{\varepsilon}} + P_{k\xi} - \bar{\varepsilon}\right), \tag{11a}$$

$$\frac{\partial}{\partial t}\left(\rho H\bar{\varepsilon}\right) + \frac{\partial}{\partial x}\left(\rho H\overline{U}\bar{\varepsilon}\right) = \frac{\partial}{\partial x}\left[\left(\mu + \frac{\bar{\xi}}{\sigma_\varepsilon}\right)H\frac{\partial \bar{\varepsilon}}{\partial x}\right] + \rho H\left(C_{1\varepsilon}\bar{k}P_H + P_{\varepsilon\xi} - C_{2\varepsilon}\frac{\bar{\varepsilon}^2}{\bar{k}}\right), \tag{11b}$$

$$P_H = 2C_\mu\left(\frac{\partial \overline{U}}{\partial x}\right)^2, \tag{11c}$$

$$P_{k\xi} = \frac{U_\tau^3}{H\sqrt{C_f}}, \tag{11d}$$

$$P_{\varepsilon\xi} = \frac{3.6C_{2\varepsilon}U_\tau^4 C_\mu^{1/2}}{H^2 C_f^{3/4}}, \tag{11e}$$

$$U_\tau = \sqrt{\frac{\tau_b}{\rho}}, \tag{11f}$$

$$\mu = \mu_w\left(1 - C_m\right) + \mu_a C_m, \tag{11g}$$

where U_τ is the boundary shear velocity; $C_f = gn_m^2/H^{1/3}$; μ_w and μ_a are the viscosities of clear water and air, respectively; and $\overline{U}(= q/H)$ is the depth-averaged horizontal velocity. The standard values of the empirical coefficients appearing in the above equations are: $C_{1\varepsilon} = 1.44$; $C_{2\varepsilon} = 1.92$; $\sigma_k = 1.0$; and $\sigma_\varepsilon = 1.30$. Equations (8)–(11g) are numerically coupled with Equations (2) and (3) for the complete solutions of the problems of skimming flow over a stepped spillway.

2.3. Air Transport Equations

The variations of air concentration in space and time are governed by the advection-diffusion equation. Compared to the vertical diffusive transport, the longitudinal one is small and can be ignored. Thus, the air transport equation for a 2D vertical plane flow can be expressed as (see, e.g., Ishii and Hibiki 2011, p. 103)

$$\frac{\partial c}{\partial t} + \frac{\partial}{\partial x}(uc) + \frac{\partial}{\partial z}(wc) + \frac{\partial}{\partial z}(w_B c) - \frac{\partial}{\partial z}\left(\xi_a \frac{\partial c}{\partial z}\right) - R_s = 0, \tag{12}$$

where c is the air concentration; w_B is the bubble rise velocity in the vertical direction; R_s is the source or sink term; and ξ_a is the air bubble diffusion coefficient in the z-direction, which is approximated by the following depth-averaged eddy-viscosity coefficient equation:

$$\xi_a = \zeta K U_\tau H, \tag{13}$$

where $\zeta = 1/6$, and K is the von Kármán constant. By integrating Equation (12) over the flow depth with the applications of Leibnitz's rule and kinematic boundary conditions, the depth-averaged air transport equation is developed as follows:

$$\frac{\partial}{\partial t}(HC_m) + \frac{\partial}{\partial x}(qC_m) + \Gamma_1 \overline{w}_B C_m - \xi_a \frac{\Gamma_2 C_m}{H} - H\overline{R}_s = 0, \tag{14}$$

where Γ_1 and Γ_2 are empirical correction coefficients accounting for the effects of turbulent diffusion and a non-uniform distribution of air concentration. The overbar in Equation (14) denotes a depth-averaged parameter. It is assumed in the derivation that the density of the air is constant.

In this study, the equation of the bubble rise velocity for a non-hydrostatic flow situation (Rutschmann et al 1986) is simplified by setting $\rho_a/\rho_w \cong 0$ (see Chanson 2013). After inserting Equation (7), the resulting simplified expression becomes

$$\overline{w}_B^2 \cong w_{B0}^2 \left(\frac{|\rho_w g H + p_D|}{\rho_w g H}\right), \tag{15}$$

where w_{B0} is the bubble rise velocity in stagnant water, which can be determined by applying empirical equations and/or design charts (see Haberman and Morton 1953, Comolet 1979). According to Kobus (1991), the effect of a bubble cloud on the rising velocity of a single bubble is less significant for a mixture flow with a horizontal velocity component, and hence, it is ignored in this work.

The source term in Equation (14) is approximately determined by the following equations for air entrainment occurring at the free surface (Hirt 2003, Souders and Hirt 2004):

$$\bar{R}_s = \frac{K_a}{\Delta H}\left(\frac{2\,(E_t - E_d)}{\rho}\right)^{1/2}, \tag{16a}$$

$$E_t = \rho\bar{k}, \tag{16b}$$

$$E_d = \rho g_n L_t + \frac{\sigma_s}{L_t}, \tag{16c}$$

$$L_t = C_t\left(\frac{3\bar{k}^3}{2\bar{\varepsilon}^2}\right)^{1/2}, \tag{16d}$$

where L_t is the turbulent length scale; E_t is the turbulent energy; E_d is the energy of gravity and surface tension; σ_s is the surface tension; $C_t = 0.0845$; K_a is a proportionality coefficient; and g_n is the component of the gravitational acceleration normal to the free surface. The process of air entrainment at the water surface is strongly influenced by the strength of the free-surface disturbance velocity resulting from the turbulent kinetic energy of the flow. When $E_t > E_d$, air is entrained into the flow at the free surface (Hirt 2003, Souders and Hirt 2004). The entrained air is distributed as a volumetric source in a layer of thickness ΔH close to the free surface, as in the approach of Ma et al (2011). This entrainment thickness can be related to some characteristic length scale of the aerated flow problem such as the flow depth at the inflow section.

At the interface between the continuous air and mixture flow, the concentration of air must be equal to 90% when air is entrained. If it surpasses this limit ($C_m > \bar{C}_{\max}$), then air detrainment will be considered by imposing a condition to control the source term as follows:

$$\bar{R}_s = \min\left[\frac{K_a}{\Delta H}\left(\frac{2\,(E_t - E_d)}{\rho}\right)^{1/2}, \Gamma_L\right], \tag{17a}$$

$$\Gamma_L \cong \frac{\bar{C}_{\max} - C_{mL}}{\Delta t}, \tag{17b}$$

where $\bar{C}_{\max}$ is the maximum value of the mean air concentration, and C_{mL} is the mean air concentration at the previous time level. The value of $\bar{C}_{\max}$ can be determined from the results of the experimental studies. The implementation of the above procedure works as a limiter for the concentration of air at the free surface.

3. Numerical Scheme

The numerical solutions of the preceding equations are obtained by using a shock-capturing finite-volume scheme, which allows simulation of flow with sharp discontinuities. The scheme is applied to the conservative form of the equations combined with a finite-difference discretization of the source terms. The main features of this scheme, such as the flux computation procedure, the predictor-corrector method for time stepping, and the implicit numerical technique, will only be briefly summarized here; further details pertaining to the numerical model can be found in Zerihun (2024).

3.1. Computation of the Numerical Flux

The flow and air transport equations can be rewritten in a vector form as follows:

$$\frac{\partial U}{\partial t} + \frac{\partial F(U)}{\partial x} = S, \tag{18}$$

where the unknown conserved variables U, the fluxes $F(U)$, and the source terms S are given by

$$U = \begin{bmatrix} H \\ q\rho \\ q\rho\left(\beta_4 \dfrac{\partial H}{\partial x} + \dfrac{\partial Z}{\partial x}\right) \\ \rho H\bar{k} \\ \rho H\bar{\varepsilon} \\ HC_m \end{bmatrix}, \tag{19a}$$

$$F(U) = \begin{bmatrix} q \\ \rho\left(\dfrac{q^2}{H}\beta_1 + \dfrac{gH^2}{2}\right) \\ \dfrac{\rho q^2}{H}\left(\beta_2 \dfrac{\partial H}{\partial x} + \beta_1 \dfrac{\partial Z}{\partial x}\right) \\ \rho q\bar{k} \\ \rho q\bar{\varepsilon} \\ qC_m \end{bmatrix}, \tag{19b}$$

$$S = \begin{bmatrix} -\frac{1}{\rho}\left(H\frac{\partial\rho}{\partial t} + q\frac{\partial\rho}{\partial x}\right) \\ -(\rho g H + p_D)\frac{\partial Z}{\partial x} - \frac{\partial}{\partial x}\left(\frac{Hp_D}{2}\right) + \frac{\partial}{\partial x}(H\bar{\sigma}_x) - \tau_b \\ p_D - \tau_b\frac{\partial Z}{\partial x} + \frac{\partial}{\partial x}(H\bar{\tau}_{zx}) + \Psi_L \\ \frac{\partial}{\partial x}\left[H\left(\mu + \frac{\bar{\xi}}{\sigma_k}\right)\frac{\partial\bar{k}}{\partial x}\right] + \rho H\left(P_{k\xi} + P_H\frac{\bar{k}^2}{\bar{\varepsilon}} - \bar{\varepsilon}\right) \\ \frac{\partial}{\partial x}\left[H\left(\mu + \frac{\bar{\xi}}{\sigma_\varepsilon}\right)\frac{\partial\bar{\varepsilon}}{\partial x}\right] + \rho H\left(P_{\varepsilon\xi} + C_{1\varepsilon}P_H\bar{k} - C_{2\varepsilon}\frac{\bar{\varepsilon}^2}{\bar{k}}\right) \\ \xi_a\frac{\Gamma_2 C_m}{H} + H\bar{R}_s - \Gamma_1\bar{w}_B C_m \end{bmatrix}, \tag{19c}$$

$$\Psi_L = \beta_3\frac{\partial}{\partial t}\left(H\rho\frac{\partial q}{\partial x} - qH\frac{\partial\rho}{\partial x}\right) + \frac{q}{2}\left(\rho\frac{\partial^2 q}{\partial x^2} + q\frac{\partial^2\rho}{\partial x^2}\right) + \frac{qH}{2}\frac{\partial}{\partial t}\left(\frac{\partial\rho}{\partial x}\right). \tag{19d}$$

After applying Euler's time stepping scheme, the discretization of the integral form of Equation (18) using the finite-volume method (Hirsch 2007, p. 208) can be written in the following form for a space-time grid:

$$U_i^{N+1} = U_i^N - \frac{\Delta t}{\Delta x}\left(F(U)_{i+1/2}^N - F(U)_{i-1/2}^N\right) + \Delta t S_i^N, \tag{20}$$

where Δx is the spatial step size in the x-direction; Δt is the time step; and i is a computational point index. In the above equation, the superscript N indicates the variables at the current time level, while $F(U)_{i\pm1/2}$ are the numerical fluxes across the interfaces of cells $i-1$, i, and $i+1$. Explicit and implicit methods are used to solve Equation (20) so as to obtain additional starting data for the proposed multi-step time integration scheme.

As a requirement for implementing the finite-volume method, the conserved variables on the cell interfaces need to be reconstructed before computing the numerical fluxes. In this study, the total variation diminishing version of a fourth-order monotone upstream centered scheme for conservation laws [MUSCL-TVD] (Yamamoto and Daiguji 1993) is used to reconstruct these variables. The weighted surface-depth gradient method (Aureli et al 2008) is employed to estimate the flow depth at the cell interfaces. This method eliminates the problem of numerical oscillations stemming from discontinues bed profile or steep bed gradient. Utilizing the reconstructed interface values, the numerical fluxes are reckoned by the Harten-Lax-van Leer (HLL) approximate Riemann solvers (Harten et al 1983) on a space-time grid. For completely solving the unknown conserved variables, ghost cells outside the boundary of the model domain are employed (LeVeque 2004, pp. 129–130). The values of the variables at these cells are extrapolated from the interior cells.

3.2. Time Stepping and Solution Methods

Using a finite-difference scheme (Bashforth and Adams 1883), the time integration is performed in the steps of predictor and corrector. In the predictor step, the third-order accurate scheme is applied to discretize the time derivative term of Equation (18), which results in the following equation:

$$U_i^P = U_i^N + \frac{\Delta t}{12}\left(23\Omega_i^N - 16\Omega_i^{N-1} + 5\Omega_i^{N-2}\right), \tag{21a}$$

$$\Omega_i = -\frac{1}{\Delta x}\left(F(U)_{i+1/2} - F(U)_{i-1/2}\right) + S_i, \tag{21b}$$

where index P stands for the predictor step, and the superscripts $N-1$ and $N-2$ are the previous time levels for the known flow conditions. In this step, Ω_i is estimated by using the values of the mixture flow variables at the known time levels in Equation (21b).

Likewise, the time integration at the corrector step is done with the fourth-order Adams–Moulton scheme by using the known cell-averaged values. Using the scheme originally proposed by Adams (Bashforth and Adams 1883), Equation (18) is discretized to yield

$$U_i^C = U_i^N + \frac{\Delta t}{24}\left(9\Omega_i^P + 19\Omega_i^N - 5\Omega_i^{N-1} + \Omega_i^{N-2}\right), \tag{22}$$

where index C refers to the corrector step. For this computational step, the value of Ω_i^P is calculated from the predicted values of the conserved variables. Because they have an especially simple structure, the equations of continuity, air transport, and turbulence model are solved explicitly at all time levels. To maintain numerical stability and accuracy, however, Equations (2) and (3) are solved implicitly for the unknown variables q and p_D at the predictor and corrector steps. Using the Adams–Moulton scheme and the finite-difference approximations (Bickley 1941) for the source terms, these momentum equations are discretized in both steps of the computation. The fluxes and source terms in the resulting equations are reckoned using the known values of the variables at the earlier time levels, thus yielding a non-linear system of equations. These implicit set of equations are first reduced from a non-linear to a linear form with the Newton–Raphson method and then solved by the lower-upper (LU) decomposition method. The technique was previously implemented to solve successfully complex flow problems (see Zerihun 2017a, 2019).

4. Results and Discussion

The characteristics of the aerated flow over a bevel-shaped stepped spillway were investigated using a non-hydrostatic depth-averaged model. As illustrated in Fig. 3, the turbulent flow below the pseudo-bottom exhibits 3D characteristics with a recirculating vortex between the faces of the step due to the effects of the macro-roughness

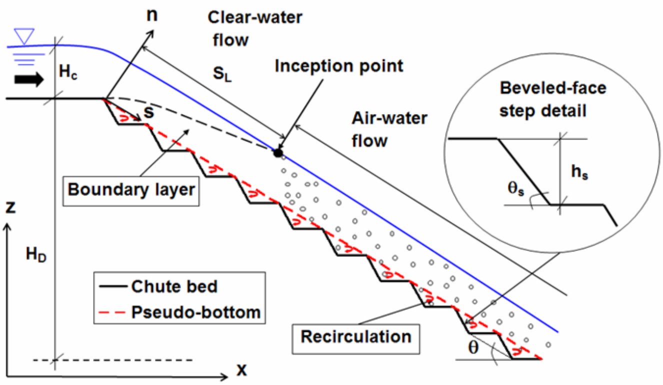

Fig. 3. Definition sketch of skimming flow over a stepped spillway with beveled-face steps. The height of the step and slope of the beveled face are indicated by h_s and θ_s, respectively. S_L denotes the streamwise distance of the free-surface inception point from the downstream edge of the weir crest

of the bed geometry. Such a complex steady flow problem was solved here as unsteady planar flow problem using time as an iteration parameter till the asymptotic final solution was attained. Experimentally determined value of S_L was used to locate the inflow section near the inception point. The flow depth, discharge, and mean air concentration were specified as boundary conditions at this section. The initial condition of the flow was assumed to be a supercritical uniform flow ($p_D = 0$) with a flow depth equal to the inflow boundary value. Additionally, the turbulent variables at this section were fixed to yield an approximate value of the eddy viscosity (see Ferziger and Peric 2002, p. 300).

For accurately simulating the mean flow characteristics of the flow problem, a small step size, which is less than 15% of the flow depth at the inflow section, was used. In addition to this, a numerical stability criterion such as the Courant–Friedrichs–Lewy (CFL) condition was used to limit the computational time step. Accordingly, a CFL value between 0.1 and 0.45 was employed to obtain stable and accurate solutions.

4.1. Relative Flow Depth Profile

The experimental data of Hunt et al (2022) were invoked to examine the model's capability for analyzing the aerated flow problem. The experiments were conducted in a near prototype scale stepped chute with a bottom slope of 18.4°. The width of the flume was 1.8 m with a vertical drop of 5.6 m. Its entrance consisted of a 3 m long broad-crested weir, which has an equivalent roughness height of 0.46 mm. The chute was provided with wooden beveled-face steps with a height of 152 mm and a face slope of 45°. A series of tests was conducted with discharges ranging from 340 to 1840 L/s/m. In the aerated region downstream of the free-surface inception point, the air-water flow properties were recorded along the centerline of the chute using a RBI dual-tip fiber optical probe. The test results reasonably satisfied the criteria recommended by Boes and Hager (2003a) for minimizing size-scale effects.

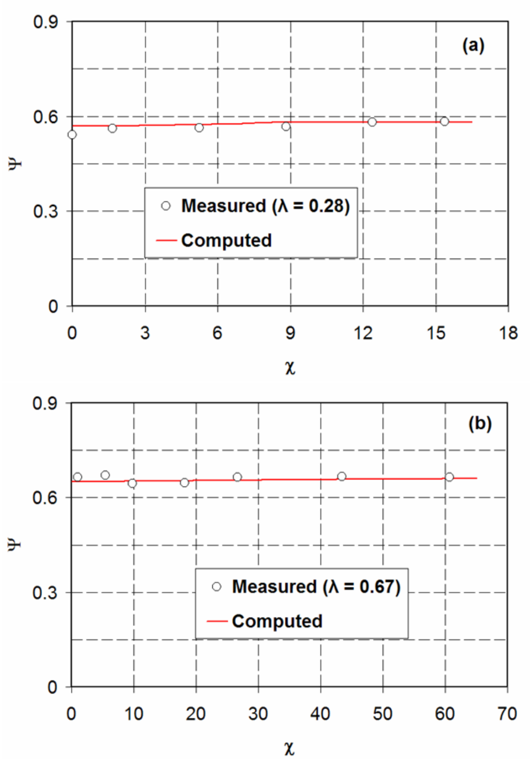

Fig. 4. Streamwise variations of the relative mixture flow depth $\Psi(\chi)$ for the discharges of (a) 1240 L/s/m and (b) 340 L/s/m. The values of the mixture flow depth relative to the pseudo-bottom were employed to predict $\Psi(\chi)$

Figure 4 shows the variation of the relative mixture flow depth Ψ (= H_n/H_c, where H_c is the critical flow depth, and H_n is the flow depth normal to the pseudo-bottom) with the normalized distance from the point of inception $\chi(= s/H_c$, where s is the streamwise distance along the pseudo-bottom) for two values of relative step height $\lambda(= h_s/H_c)$. For both low and high flows, the numerical results closely correlated with the experimental data, demonstrating the model's capacity for capturing the effects of air entrainment on the local flow characteristics. The mean absolute relative error (MARE) in the computed results was 2%. The simulated profiles were nearly horizontal throughout the aerated flow zone, confirming the prevalence of a quasi-uniform flow situation in this zone. For such a quasi-hydrostatic flow, the effect of the vertical acceleration is insignificant, except in the region close to the bottom of the chute.

4.2. Mean Air Concentration

The streamwise variation of the computed mean air concentration for low and high flows is presented in Fig. 5. The numerical model slightly underestimated the mean air concentration, especially in the flow region close to the toe of the spillway. This discrepancy is attributed to the 3D effects of the aerated flow as well as the implementation of inappropriate experimental procedure (only suitable for data measured in the streamwise and transverse directions for the cross-section averaging method) for the location of the free-surface inception point, which overestimates the S_L values. As shown in the figure, the mean air concentration gradually increased in the aerated flow region, approaching an equilibrium concentration. This trend was satisfactorily predicted by the model with a MARE of 7.3%. It is clear from Fig. 5 that the mean air concentrations are higher for the lower discharge, as previously noted by Straub and Anderson (1960) for smooth chute flows under a non-equilibrium condition. This signifies that for the higher discharge, the turbulent flow may not be a fully-developed

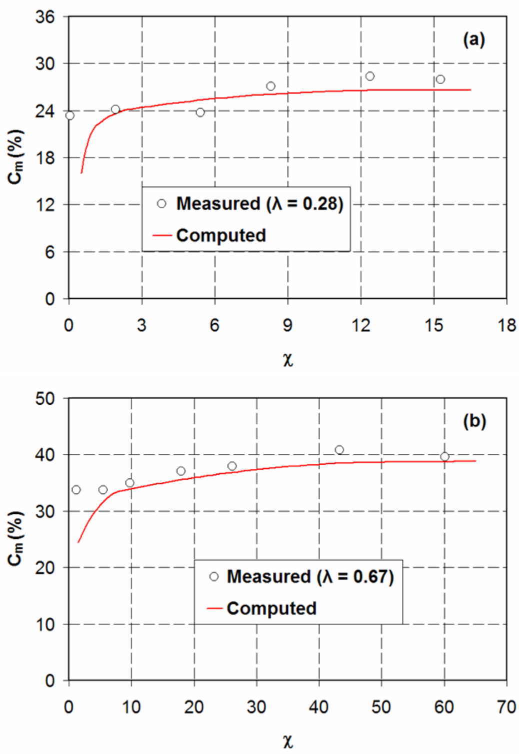

Fig. 5. Mean air concentration versus non-dimensional distance from point of inception for a skimming flow over a stepped chute: (a) q = 1240 L/s/m; and (b) q = 340 L/s/m. The mean values were computed using flow depths with an upper limit air concentration of 90%

aerated flow before the outflow section. Taking into consideration the complex 3D characteristics of the problems of air-water flow, the results of the depth-averaged model were satisfactory.

4.3. Energy Dissipation Rate

The above numerical results were further analyzed to compute the relative energy loss, ε_L, between the critical and downstream sections. The equation for flow in a steep slope channel (see Zerihun 2017b) can be applied to obtain the relative energy loss between these sections. The resulting expression for an ungated structure reads as

$$\begin{aligned}\varepsilon_L &= \frac{\Delta E}{E_{0,i}} \\ &= 1 - \frac{(1 - C_{m,i})\, H_i \cos^2\theta}{1.5H_c + (H_D - Z_i)} - \frac{\alpha_i}{2g\,(1.5H_c + (H_D - Z_i))}\left(\frac{q_w}{(1 - C_{m,i})H_i \cos\theta}\right)^2,\end{aligned} \tag{23}$$

where ΔE is the energy loss between the critical section and a downstream section at node i; H_D is the spillway height above the toe; Z_i is the bed elevation of a section at node i; q_w is the clear-water discharge per unit width; α_i is the Coriolis velocity correction coefficient, which can be estimated by empirical equations (e.g., Hunt et al 2014); and $E_{0,i}$ is the total energy head at the critical section relative to the downstream section at node i. By considering the critical and the downstream end sections, the following expression for the relative total energy loss (ε_T) is obtained:

$$\begin{aligned}\varepsilon_T &= \frac{\Delta E}{H_D} \\ &= 1 + 1.5\Gamma_D^{1/3} - \left[(1 - C_m)_M \Psi_M \cos\theta + \frac{\alpha_M}{2}\left(\frac{1}{(1 - C_m)_M \Psi_M}\right)^2\right]\Gamma_D^{1/3},\end{aligned} \tag{24}$$

where $\Gamma_D \left(= q^2/gH_D^3\right)$ is the drop number, and the subscript M denotes flow variables at the outflow section.

Figure 6 compares the numerical results with the experimental data of Hunt et al (2022) for low and high flows. For both flows, the relative energy loss increases in the streamwise direction and attains its maximum value near the toe of the stepped chute. As can be seen, the model adequately simulates the increasing trend of the energy dissipation rate with a MARE of 8.5%. Comparison of the results of the two flows reveals that for the higher discharge, the relative energy loss is higher at the free-surface inception point (see Fig. 6a). This is due to the fact that increasing the discharge shifts the point of incipient aeration further downstream toward the outflow section, which in turn increases the number of energy dissipating steps. At the toe of the spillway, the result of the lower discharge shows a lower residual energy.

In Fig. 7, the computed relative total energy loss is compared with the experimental data (Hunt et al 2022, Megh Raj and Crookston 2024). Megh Raj and Crookston

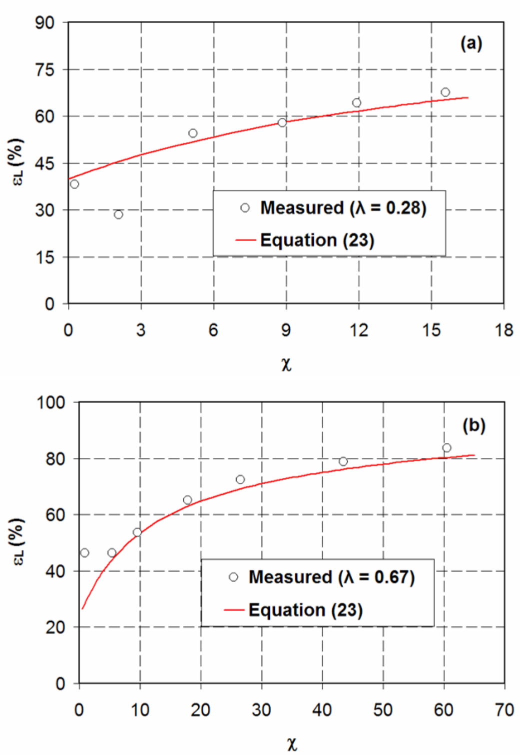

Fig. 6. Streamwise variation of the relative energy loss $\varepsilon_L(\chi)$: (a) q = 1240 L/s/m; and (b) q = 340 L/s/m. The numerical results are compared with the experimental data of Hunt et al (2022)

performed similar experiments by using a stepped chute with a bottom slope of 18.4° and a vertical drop of 1.8 m. They tested two beveled-face steps, each having a face slope of 45° and heights of 100 and 200 mm. The air-water flow properties for λ varying from 0.32 to 0.86 were measured using a dual-tip phase detection conductivity probe at the downstream end section. As shown in the figure, the agreement between the numerical and the experimental results is satisfactory with a MARE of 2%. Furthermore, the energy dissipation rate decreases as the drop number increases. The overall results reveal that an increase in discharge leads to a decrease in the energy dissipation rate of the bevel-shaped stepped spillway. This is because of the substantial decrease of the form drag induced by the steps at higher discharge, which compensates for the effect of skin friction in increasing the dissipation rate especially in the non-aerated zone. For such a peak discharge, the turbulent mixture flow may not reach an equilibrium condition at the downstream end section. The present results are consistent with the results of an earlier study (Boes and Hager 2003b) for skimming flow over a stepped spillway with vertical face steps.

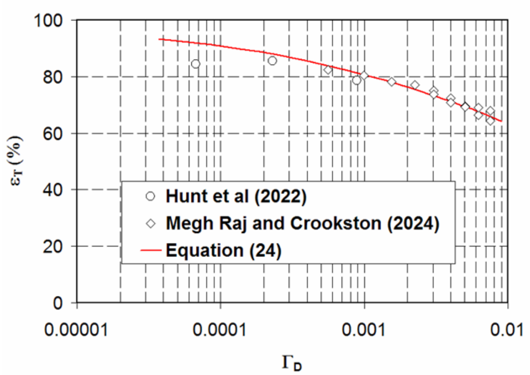

Fig. 7. The relative total energy loss at the toe of a stepped chute ε_T as a function of the drop number Γ_D

5. Conclusions

This study describes the results of a numerical investigation aimed at predicting the air-water flow properties and energy dissipation rate of skimming flow over a moderately sloping stepped spillway with beveled-face steps. A non-hydrostatic depth-averaged mixture flow model, which couples the Boussinesq-type equations with the depth-averaged air transport equations, was employed to analyze the planar two-dimensional flow problem. The effects of turbulence on the aerated flow were also accounted for by implementing a depth-averaged $k - \varepsilon$ turbulence model. A hybrid finite-volume and finite-difference scheme was employed to discretize and solve the non-linear equations of the model. All these special features of the model's structure make the current model quite different from the previous lower-order energy equation-based model. Its numerical results were validated using a set of data from the experiments which were conducted in a near prototype scale stepped chute.

For both low and high flows, the numerical results closely correlated with the experimental data, thereby demonstrating the model's capacity for capturing the effects of air entrainment on the dynamic characteristics of the flow. In the flow region close to the toe of the spillway, a minor discrepancy between the numerical and experimental results for the mean air concentration was observed. This discrepancy is attributed to the complex three-dimensional characteristics of the aerated flow, which cannot be accurately portrayed by the depth-averaged model. Analysis of the comparison results revealed that the profiles of the relative flow depth were nearly horizontal throughout the aerated flow zone, confirming the prevalence of a quasi-uniform flow situation in which the curvatures of the streamline are insignificant. Additionally, the energy dissipation performance of the stepped spillway was examined. The results showed that the total energy loss decreases as the drop number increases, which is similar to the general trend of the rate of energy dissipation with increasing discharge. With the established acceptable accuracy, the proposed model is favorably suited to analyzing the mean flow characteristics of an open-channel bubbly flow in a stepped chute with beveled-face steps, and hence, it has the potential to be used as an engineering tool to evaluate the conceptual design of embankment dam stepped spillways.

Notation

c	–	air concentration (–)
C	–	corrector step index (–)
C_m	–	mean air concentration (–)
C_{mL}	–	mean air concentration at the previous time step (–)
$\bar{C}_{\max}$	–	maximum value of the mean air concentration (–)
E_d	–	energy of gravity and surface tension ($ML^{-1}T^{-2}$)
E_t	–	turbulent energy ($ML^{-1}T^{-2}$)
$E_{0,i}$	–	total energy head at the critical section relative to node i (L)
g	–	gravitational acceleration (LT^{-2})
g_n	–	component of gravitational acceleration normal to the free surface (LT^{-2})
h_s	–	height of the step (L)
H	–	mixture flow depth (L)
H_c	–	critical depth (L)
H_D	–	spillway height (L)
H_n	–	flow depth normal to the pseudo-bottom (L)
i	–	computational point index (–)
$\bar{k}$	–	depth-averaged turbulent kinetic energy (L^2T^{-2})
L_t	–	turbulent length scale (L)
n	–	coordinate normal to the pseudo-bottom (L)
n_m	–	Gauckler–Manning roughness coefficient ($L^{-1/3}T$)
N	–	time level (–)
p	–	total pressure ($ML^{-1}T^{-2}$)
p_D	–	dynamic bed pressure ($ML^{-1}T^{-2}$)
P	–	predictor step index (–)
q	–	aerated flow discharge per unit width (L^2T^{-1})
q_w	–	clear-water discharge per unit width (L^2T^{-1})
R_H	–	hydraulic radius (L)
R_s	–	source or sink term (T^{-1})
s	–	streamwise distance along the pseudo-bottom (L)
S_L	–	distance of the inception point from the edge of the crest (L)
t	–	time (T)
u	–	horizontal velocity (LT^{-1})
$\bar{U}$	–	depth-averaged horizontal velocity (LT^{-1})
U_τ	–	shear velocity (LT^{-1})
w	–	vertical velocity (LT^{-1})

w_B – bubble rise velocity (LT^{-1})
w_{B0} – bubble rise velocity in stagnant water (LT^{-1})
x, y, z – Cartesian coordinates (L)
Z – channel bed elevation (L)
α – Coriolis coefficient (–)
Γ_D – drop number (–)
Γ_1, Γ_2 – empirical correction coefficients (–)
ΔE – energy loss (L)
ΔH – thickness of a water layer (L)
Δt – time step (T)
Δx – spatial step size (L)
$\bar{\varepsilon}$ – dissipation rate of turbulent kinetic energy (L^2T^{-3})
ε_L – relative energy loss (–)
ε_T – relative total energy loss (–)
η – free-surface elevation (L)
θ – slope of the bottom of the chute (deg)
θ_s – slope of the beveled face (deg)
λ – relative step height (–)
Λ – normalized vertical coordinate (–)
μ – dynamic viscosity of air-water mixture ($ML^{-1}T^{-1}$)
μ_a – dynamic viscosity of air ($ML^{-1}T^{-1}$)
μ_w – dynamic viscosity of clear water ($ML^{-1}T^{-1}$)
$\bar{\xi}$ – depth-averaged eddy viscosity ($ML^{-1}T^{-1}$)
ξ_a – air bubble diffusion coefficient (L^2T^{-1})
ρ – density of air-water mixture (ML^{-3})
ρ_a – density of air (ML^{-3})
ρ_w – density of clear water (ML^{-3})
σ_s – surface tension (MT^{-2})
$\overline{\sigma}_x$ – depth-averaged normal stress ($ML^{-1}T^{-2}$)
τ_b – bed shear stress ($ML^{-1}T^{-2}$)
$\bar{\tau}_{zx}$ – depth-averaged tangential stress ($ML^{-1}T^{-2}$)
χ – normalized streamwise distance (–)
Ψ – relative mixture flow depth (–)
ω – velocity distribution parameter (–)

References

Almeland S. K., Mukha T., Bensow R. E. (2021) An improved air entrainment model for stepped spillways, *Appl. Math. Model.*, **100**, 170–191.

Aureli F., Maranzoni A., Mignosa P., Ziveri C. (2008) A weighted surface-depth gradient method for the numerical integration of the 2D shallow-water equations with topography, *Adv. Water Resour.*, **31**(7), 962–974.

Bashforth F., Adams J. C. (1883) *An Attempt to Test the Theories of Capillary Action by Comparing the Theoretical and Measured Forms of Drops of Fluid, with an Explanation of the Method of Integration Employed in Constructing the Tables which Give the Theoretical Forms of Such Drops*, Cambridge University Press, Cambridge, UK, 18–19.

Bayon A., Toro J. P., Bombardelli F. A., Matos J., Lopez-Jimenez P. A. (2018) Influence of VOF technique, turbulence model and discretization scheme on the numerical simulation of the non-aerated, skimming flow in stepped spillways, *J. Hydro-Environ. Res.*, **19**, 137–149.

Bickley W. G. (1941) Formulae for numerical differentiation, *Math. Gaz.*, **25**(263), 19–27, doi:10.2307/3606475.

Boes R. M., Hager W. H. (2003a) Two-phase flow characteristics of stepped spillways, *J. Hydraul. Eng.*, **129**(9), 661–670.

Boes R. M., Hager W. H. (2003b) Hydraulic design of stepped spillways, *J. Hydraul. Eng.*, **129**(9), 671–679.

Bombardelli F. A., Meireles I., Matos J. (2011) Laboratory measurements and multi-block numerical simulations of the mean flow and turbulence in the non-aerated skimming flow region of steep stepped spillways, *Environ. Fluid Mech.*, **11**(3), 263–288.

Boussinesq J. (1877) *Essai Sur la Théorie des Eaux Courantes* [*Essay on the Theory of Water Flow*], Mémoires Présentés par Divers Savants à l'Académie des Sciences, Paris, **23**(1), 1–680 [in French].

Castro A. M., Li J., Carrica P. M. (2016) A mechanistic model of bubble entrainment in turbulent free-surface flows, *Int. J. Multiph. Flow*, **86**, 35–55.

Chanson H. (1994) Drag reduction in open-channel flow by aeration and suspended load, *J. Hydraul. Res.*, **32**(1), 87–101.

Chanson H. (2013) Advective diffusion of air bubbles in turbulent water flows, In: *Fluid Mechanics of Environmental Interfaces*, Taylor and Francis, Leiden, The Netherlands, Gualtieri, C. and Mihailovic, D. T. (eds.), 2nd ed., Chapter 7, 181–219.

Chinnarasri C., Wongwises S. (2004) Flow regimes and energy loss on chutes with upward inclined steps, *Can. J. Civ. Eng.*, **31**, 870–879.

Comolet R. (1979) Sur le Mouvement d'une bulle de gaz dans un liquide [Gas bubble motion in a liquid medium], *La Houille Blanche*, **65**(1), 31–42 [in French].

Ferziger J. H., Peric M. (2002) *Computational Methods for Fluid Dynamics*, 3rd rev. ed., Springer-Verlag Berlin Heidelberg: New York, NY, USA.

Haberman W. L., Morton R. K. (1953) *An Experimental Investigation of the Drag and Shape of Air Bubbles Rising in Various Liquids*, Report 802, Armed Services Technical Information Agency, Dayton, OH, USA.

Hansen K. D., Fitzgerald T. J. (2016) Performance of RCC used for overtopping protection and spillways, *Proceedings of the 2nd International Seminar on Dam Protection against Overtopping*, Fort Collins, CO, USA, 7–9 Sept., 1–11.

Harten A., Lax P. D., van Leer B. (1983) On upstream differencing and Godunov-type scheme for hyperbolic conservation laws, *SIAM Rev. Soc. Ind. Appl. Math.*, **25**(1), 35–61.

Hirsch C. (2007) *Numerical Computation of Internal and External Flows: Vol. 1 Fundamentals of Computational Fluid Dynamics*, 2nd ed., Elsevier: Oxford, UK.

Hirt C. W. (2003) Modeling turbulent entrainment of air at a free surface, *Technical Note 61 (FSI-03-TN61)*, Flow Science Incorporated, Santa Fe, NM, USA.

Hunt S. L., Kadavy K. C., Hanson G. J. (2014) Simplistic design methods for moderate-sloped stepped chutes, *J. Hydraul. Eng.*, **140**(12), doi:10.1061/(ASCE)HY.1943-7900.0000938.

Hunt S. L., Kadavy K. C., Wahl T. L., Moses D. W. (2022) Physical modeling of beveled-face stepped chute, *Water*, **14**(3), doi:10.3390/w14030365.

Ishii M., Hibiki T. (2011) *Thermo-Fluid Dynamics of Two-Phase Flow*, 2nd ed., Springer Science and Business Media, LLC: New York, NY, USA.

Jones W. P., Launder B. (1972) The prediction of laminarization with a two-equation model of turbulence, *Int. J. Heat Mass Transf.*, **15**, 301–314.

Kobus H. (1991) Introduction to air-water flows, In: *Air Entrainment in Free-Surface Flows*, IAHR Hydraulic Structures Design Manual No. 4, Hydraulic Design Considerations, Wood, I. R. (ed.), Balkema, Rotterdam, The Netherlands, 1–28.

LeVeque R. J. (2004) *Finite-Volume Methods for Hyperbolic Problems*, Cambridge University Press: Cambridge, UK.

Lopes P., Leandro J., Carvalho R. F. (2017) Self-aeration modeling using a sub-grid volume of fluid model, *Int. J. Nonlinear Sci. Numer. Simul.*, **18**(7–8), 559–574.

Ma J., Oberai A. A., Drew D. A., Lahey R. T., Hyman M. C. (2011) A comprehensive sub-grid air entrainment model for RANS modeling of free-surface bubbly Flows, *J. Comput. Multiph. Flows*, **3**(1), 41–56.

Megh Raj K. C., Crookston B. (2024) A laboratory study on the energy dissipation of a beveled-face stepped spillway for embankment dam applications, *Proceedings of the 10th International Symposium on Hydraulic Structures*, Zürich, Switzerland, 17–19 June, 530–537.

Rastogi A. K., Rodi W. (1978) Prediction of heat and mass transfer in open channels, *J. Hydraul. Div.*, **104**(HY3), 397–420.

Relvas A. T., Pinheiro A. N. (2008) Inception point and air concentration in flows on stepped chutes lined with wedge-shaped concrete blocks, *J. Hydraul. Eng.*, **134**(8), 1042–1051.

Rutschmann P., Volkart P., Wood I. R. (1986) Air entrainment at spillway aerators, *Proceedings of the 9th Australasian Fluid Mechanics Conference*, Auckland, New Zealand, 8–12 Dec., 350–353.

Sene K. J. (1988) Air entrainment by plunging jets, *Chem. Eng. Sci.*, **43**(10), 2615–2623.

Souders D. T., Hirt C. W. (2004) Modeling entrainment of air at turbulent free surfaces, *Proceedings of World Water and Environmental Resources Congress*, Salt Lake City, UT, USA, 27 June–1 July, 1–10.

Straub L. G., Anderson A. G. (1960) Self-aerated flow in open channels, *Trans. ASCE*, **125**(1), 456–481.

Wahl T. L., Falvey H. T. (2022) SpillwayPro: Integrated water surface profile, cavitation, and aerated flow analysis for smooth and stepped chutes, *Water*, **14**(8) doi:10.3390/w14081256.

Yakhot V., Orszag S. A. (1986) Renormalization group analysis of turbulence. I. Basic theory, *J. Sci. Comput.*, **1**(1), 3–51.

Yamamoto S., Daiguji H. (1993) Higher-order accurate upwind schemes for solving the compressible Euler and Navier-Stokes equations, *Comput. Fluids*, **22**(2–3), 259–270.

Zabaleta F., Márquez-Damián S., Bombardelli F. A. (2023) A novel three-phase mixture approach for the numerical modeling of self-aerated flows, *Comput. Methods Appl. Mech. Engrg.*, **408**, doi:10.1016/j.cma.2023.115958.

Zerihun Y. T. (2016) Modeling free-surface flow with curvilinear streamlines by a non-hydrostatic model, *J. Hydrol. Hydromech.*, **64**(3), 281–288.

Zerihun Y. T. (2017a) A numerical study of non-hydrostatic shallow flows in open channels, *Arch. Hydro-Eng. Environ. Mech.*, **64**(1), 17–35.

Zerihun Y. T. (2017b) A non-hydrostatic depth-averaged model for hydraulically steep free-surface flows, *Fluids*, **2**(4), doi:10.3390/fluids2040049.

Zerihun Y. T. (2019) On steady two-dimensional free-surface flows with spatially-varied discharges, *Slovak J. Civ. Eng.*, **27**(3), 1–11.

Zerihun Y. T. (2021) Non-hydrostatic transitional open-channel flows from a supercritical to a subcritical state, *Slovak J. Civ. Eng.*, **29**(2), 39–48.

Zerihun Y. T. (2024) Numerical modeling of sediment transport and bed evolution in nonuniform open-channel flows, *Arch. Hydro-Eng. Environ. Mech.*, **71**(1), 1–26.

Zhang G., Chanson H. (2018) Effects of step and cavity shapes on aeration and energy dissipation performances of stepped chutes, *J. Hydraul. Eng.*, **144**(9), doi:10.1061/(ASCE)HY.1943-7900.0001505.